# Nano-Confined Crystallization in Poly(lactic acid) (PLA) and Poly(ethylene terephthalate) (PET) Induced by Various Forms of Pre-melt-deformation

Travis Smith[1], Jiansheng Feng[1], Lu Zou[2], Min Gao[2], Marianne Prévôt[2], and Shi-Qing Wang[1,*]

[1] School of Polymer Science and Polymer Engineering, University of Akron, Ohio 44325

[2] Advanced Materials and Liquid Crystal Institute, Kent State University, Ohio 44242

**Abstract**

We explore the processing-structure-property relationship using poly(lactic acid) (PLA) and poly(ethylene terephthalate) (PET). Specifically, we show both pre-extension and pre-shear of amorphous PLA and PET above their glass transition temperatures $T_g$, carried out in the affine deformation limit, can induce a specific type of cold crystallization during annealing, i.e., nano-confined crystallization (NCC) where crystal sizes are limited to a nanoscopic scale in all dimensions so as to render the processed PLA and PET optically transparent. The new polymer structure after pre-melt deformation can show considerably enhanced mechanical properties. For example, pre-melt stretching produces geometric condensation of the chain network. This structural alternation can profoundly change the mechanical characteristics, e.g., turning brittle PLA ductile. In contrast, after pre-shear of amorphous PLA above $T_g$, the NCC containing PLA remains brittle, showing the importance to have geometric condensation from processing. Both AFM imaging and SAXS measurements have been carried to verify that pre-melt deformation of PLA and PET indeed results in NCC from annealing that permits the strain-induced cold crystallization to take place on the length scale of the mesh size of the deformed chain network.

* corresponding author at swang@uakron.edu

This article has been accepted for publication and undergone full peer review but has not been through the copyediting, typesetting, pagination and proofreading process, which may lead to differences between this version and the Version of Record. Please cite this article as doi: 10.1002/marc.202200293.

## 1. Introduction

Petrochemical polymers like polyethylene (PE), polypropylene (PP), and poly(ethylene terephthalate) (PET) have gained wide applications because of their outstanding mechanical and thermal properties. A growing urgency to shift to sustainable polymers like poly(lactic acid) (PLA) and poly(hydroxyalkanoate) (PHA) has made it necessary to ask: (1) why PLA and PHA have such poor mechanical characteristics, and (2) how to improve their mechanical properties so that they become desirable, e.g., adequate to compete with or surpass PET and PE, respectively.

From the existing phenomenology of the mechanical behaviors of such polymers, it appears certain that crystallization can disrupt the chain network. Since there is no chain crossing in lamellae, slow crystallization may deplete chain uncrossability. In fact, at sufficiently high crystallinity even HDPE is brittle.[1] In the presence of large spherulites, PP can also become non-drawable.[2] Moreover, with reduced chain uncrossability due to crystallization, even freshly prepared crystalline PLA is completely brittle while amorphous PLA can be temporarily ductile – before physical aging causes PLA to turn brittle.[3] Ten degrees below $T_g$, PP is also brittle,[4] consistent with the speculation that crystallization has a detrimental effect on polymer ductility since Vincent had reported[5] the brittle-ductile transition temperature equal to −120 °C for PP that was presumably prepared with minimal crystallization.

Both PLA and PET have $T_g$ well above room temperature, and show slow crystallization kinetics.[6] Therefore, they can be prepared in the amorphous state by quick thermal quenching. Upon annealing of these amorphous polymers above $T_g$, they are temporarily in the disordered state, i.e., melt state. Pre-melt deformation refers to deformation before any crystallization. Brittle glassy polymers like PLA can be made ductile by pre-melt stretching to produce geometric condensation[7, 8] of the chain network.[9] Moreover, pre-melt stretched PLA can crystallize upon annealing above $T_g$ to undergo strain-induced nano-confined crystallization (NCC).[3] Such constrained crystallization takes place on the length scale defined by the meshes of the stretched chain network and cannot grow to micron sized lamellae because of the limited mass transport. Unlike conventional isotropic crystallization where the dimension transverse to the lamellar thickness can be as large as tens of microns, this NCC state affords PLA optical transparency and high heat-distortion temperature. Such behavior is not limited to PLA, as pre-melt stretched PET can also be crystallized in similar manner.[10]

The melt-deformation-induced NCC is a different concept from that of nano-oriented crystal (NOC), which has been explored earlier in the literature.[11, 12] The formation of NCC is generated within the limit of preserving the entanglement network, which is achieved under the affine deformation condition, i.e., at high Weissenberg number ($Wi \gg 1$) during stepwise deformation. Such a protocol is rather different from that involved in the topic of flow-induced crystallization (FIC) of polymers.[13-16] The previous report of NOC in PET belongs to the same topic of FIC where melt deformation takes place above, or at or near $T_c$ (i.e., ca. 240 °C). At such a high temperature, NOC was observed to occur only at sufficiently high Hencky rate (above 150 $s^{-1}$) where only the longest chains may have slow chain relaxation to be stretched to induce crystallization.

The present study also differs from the vast literature[17-21] on structural changes[22-25] due to ductile deformation of polymers in their semicrystalline state. Our objective is to investigate whether, how and why pre-melt deformation of different forms (e.g., shear vs. extension) can induce NCC and result in improved mechanical characteristics based on PLA and PET. Specifically, we show that although NCC take places after annealing of pre-melt-deformed PLA, pre-melt shearing does not make PLA ductile unlike the effect of pre-melt stretching that produces geometric condensation[8] of the chain network, a concept briefly discussed in Section 2.

## 2. Technical considerations and analyses

To perform pre-melt deformation on glassy PLA and PET, which must take place above room temperature, we employ a home-made device as depicted in Fig. 1, where squeezing forces the specimen to exit at the two openings at either end of the trough. This setup can be fit into an oven built for Instron tensile testers and has previously been used without[26] and with lubrication[27] in both creep and displacement-controlled modes to produce different types of deformation, from shear to planar extension. In other words, with slip-like boundary condition produced by lubrication we achieve planar extension; with no-slip boundary condition, the melt deformation during compression can be shown to be dominantly shear. While the explicit strain field cannot be prescribed without a constitutive equation, it can be shown[8] that the velocity field is the same for either Newtonian liquids or Hookean solids.

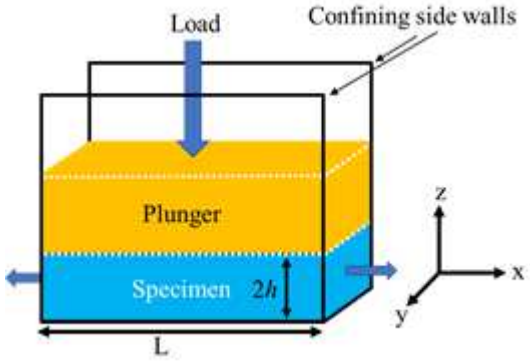


**Figure 1** Sketch of the squeezing device for shear involving a sample with length L, fixed width W, and height H. The coordinate system has its origin in the center, with the boundaries defined by x = ± L/2, y = ± W/2, and z = ± *h*.

The following analysis should apply in the limit of linear viscoelasticity. The analysis allows us to estimate the degree of melt deformation and corresponding stress as well as the pressure due to the squeezing. It can be shown[8] that the velocity along the X axis grows with x and is parabolic with respect to the sample height, given by

$$v_x(x,z) = (3/2)(\dot{\quad} \qquad z/h)^2] \tag{1}$$

whose derivative with respect to z shows spatially varying shear rate

$$\dot{\quad} \qquad , \tag{2}$$

where 2*h* is the height of the specimen at time *t*, $2\dot{h}$ is the squeezing speed and $\dot{\varepsilon}$ is the maximum extensional rate. The variation of $v_x$ with x indicates there is also extensional deformation in this squeeze setup, with the maximum rate of extension in the middle of specimen, given by

$$\dot{\varepsilon} = \frac{\partial v_x(x, z=0)}{\partial x} = (3/2)(\dot{h}/h) \quad . \tag{3}$$

When the squeezing is conducted to keep $\dot{\varepsilon} \sim \dot{h}/h$ constant so that $h(t) = h_0\exp[-(\dot{h}/h)t]$, the maximum extension ratio $\lambda_{max}$ is related to the squeeze ratio $h_0/h$ as

$$\lambda_{max} = \exp(\dot{\varepsilon}\,t) = (h_0/h)^{3/2}. \tag{4}$$

At x = L/2, the maximum shear rate is given by

$$\dot{\gamma} = \dot{\varepsilon}\left(\frac{h_0}{h} - \frac{h}{h_0}\right) \approx \dot{\varepsilon}\frac{h_0}{h} = \frac{3}{2}\frac{L}{h}\frac{\dot{h}}{h}, \tag{5}$$

where the last equality holds for $L/h_0 >> 1$ and $h_0 > h$. The fact that $\dot{\gamma} \gg \dot{\varepsilon}$ allows us to impose approximate shear melt deformation in the elastic limit, i.e., with Weissenberg number $Wi_{shear} = \dot{\gamma}\tau >> 1$, but not elastic extension because of $Wi_{extension} = \dot{\varepsilon}\tau \leq 1$.

It can be shown in the elastic limit[8] that the squeezing produces a total shear strain at a given squeezing ratio $h_0/h$

$$\gamma(x,z) = (3/2)(xz/h_0^2)[(h_0/h)^2 - 1], \tag{6}$$

which reaches maximum at x = ±L/2 and z = ±*h*

$$\gamma_{max} = (¾)(L/h_0)(h_0/h - h/h_0), \tag{7}$$

where use is made of Eq. (4). Thus, both Eqs. (5) and (7) show that shear deformation is greater than extensional deformation by a factor $L/h_0$. Corresponding to $\gamma_{max}$, the maximum shear stress $\sigma_{zx(max)} = G_{pl}\gamma_{max}$ is related[8] to the squeezing pressure P as

$$\sigma_{zx(max)} = (6h/L)P. \tag{8}$$

The velocity field given by Eq. (1) assumes a no-slip boundary condition: $v_x(z = \pm h) = 0$. Although wall slip only occurs in well entangled melts, it is hard to avoid it in the present setting. To avoid cold crystallization of amorphous PLA and PET in presence of pre-melt squeezing, the squeezing is performed 10-20 degrees above $T_g$, where there is insufficient molecular mobility required for crystallization.[3],[28] Polymer adsorption and cold crystallization both take time to develop. Such low temperatures do not allow complete chain absorption. Poor contact between the samples and the two surfaces of XY plane could produce a partial slip boundary condition.

The extent of slip during squeeze may be quantified by marking the specimen's surface with black lines as shown in the photos in Fig. 2(a)-(b), which are the examples of PLLA and PET after squeezing to $h_0/h$ = 2.0 and 1.8, respectively With $x_0$ denoting the initial positions of the marks and

$\Delta x = x - x_0$ representing the displacement of the marks, in Fig. 2(a)-(b), we show the level of deviation from the no-slip boundary condition. Fig. 2(a) involves two values of L = 27 and 55 mm, respectively. Also drawn in Fig. 2(a)-(b) are the dashed lines for the case of planar extension, given in terms of the squeezing ratio $h_0/h$: $\Delta x/x = h_0/h - 1$.

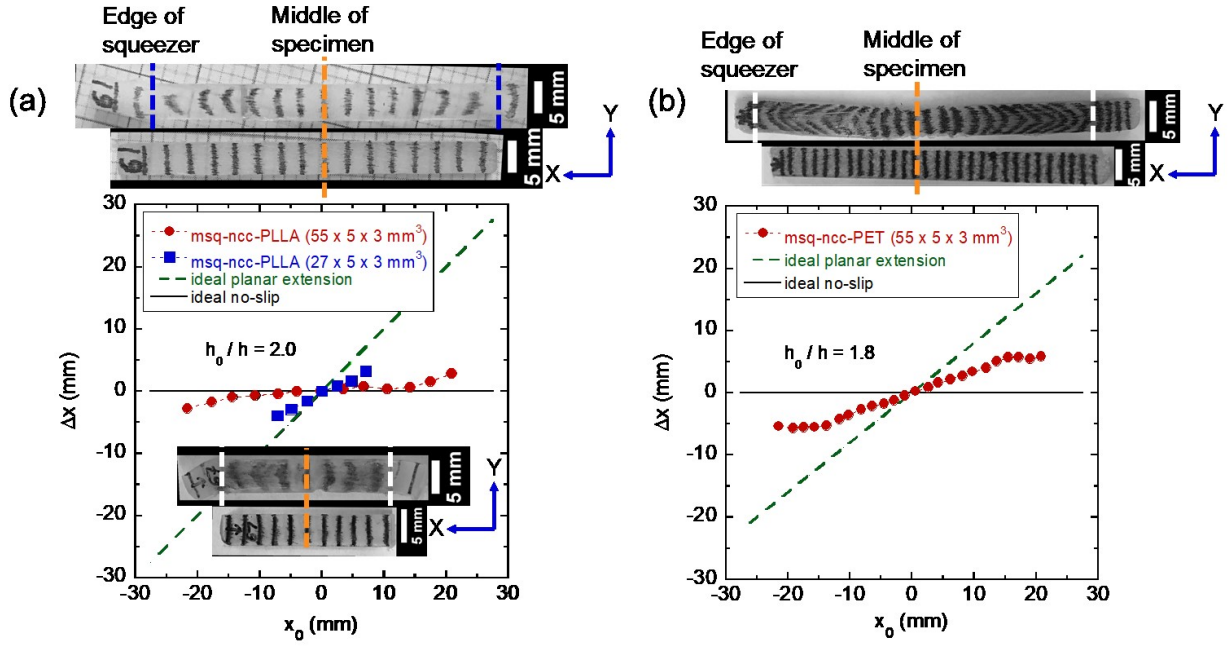


**Figure 2** Extent of slip from squeezing of the PLLA (a) and PET (b) specimens from Figs. 6(b), 7(b), and 8. The specimen dimensions ($L_0 \times W_0 \times 2h_0$) are indicated in the plot legends. Photographs of the specimens prior to- and post-deformation are placed side-by side. Only the material remaining within the device remains deformed; the excess deformed material "shrinks" due to lack of constraint above $T_g$ and defines the edge of the squeezing device (marked with white and blue dashed lines). The center defines the middle of the specimen (marked with orange dashed lines); the ink mark in the post-deformed specimen is compared to the corresponding pre-deformation mark in order to determine the net displacement $\Delta x$ of that mark as a result of deformation. The $\Delta x$ is plotted as a function of the initial position of the mark prior to deformation $x_0$. The curves are bounded by the two extremes: no-slip (black solid line at $\Delta x = 0$) and planar extension (green dashed line). It is clear that the longer ($L_0$ = 55 mm) PLLA specimen experienced little slip except near the edges of the device, in contrast to the shorter PLLA specimen and the long PET specimen.

It is necessary to indicate the contrast of pre-shear effect achieved through the squeezing apparatus (Fig. 1) with that of uniaxial melt stretching. Shear deformation differs from uniaxial extension in a fundamental way. The loading cross-section (YZ plane) contracts during uniaxial extension. Consequently, as shown in Fig. 3, there are more load-bearing strands (LBSs) per unit cross-sectional area after the melt stretching, as LBSs (represented by solid circles in YZ plane) become less coiled. Here we note that the LBSs being Gaussian coils is the cause for why the areal density of LBSs is low relative to the fully stretched state where all LBSs are straightened, attaining maximum geometric condensation,[8] approximately achievable through efficient fiber spinning. In contrast, the shear plane (XY) and the height of the specimen remain unchanged during shear, as

illustrated in Fig. 3, such that the loading plane (YZ) attains no geometric condensation from affine pre-shear deformation.

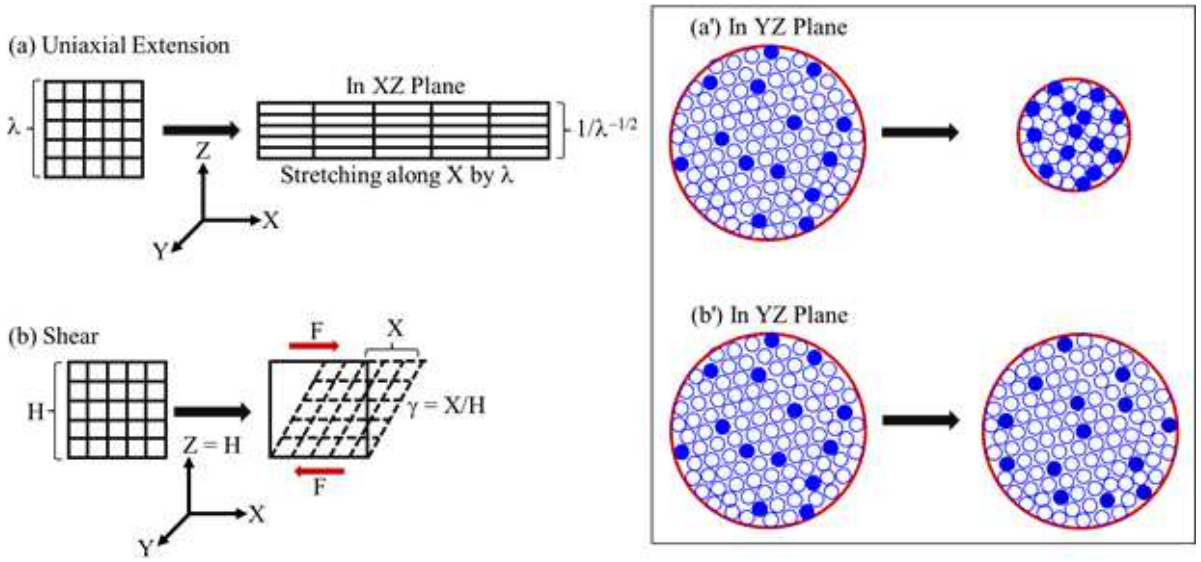


**Figure 3** Entangled polymer of initial length $X_0$, width $Y_0$ and thickness (extension) or height (shear) $Z_0$ in the melt state with Gaussian entanglement strands denoted by straight lines that intersect at points of uncrossability. During affine uniaxial extension (a) along X, the chain network elongates along X by draw ratio $\lambda = (X_0 + X)/X_0$ and contracts in both Y and Z by $\lambda^{-1/2}$. (a') The contraction of the cross-sectional area YZ brings the load-bearing strands (solid circles) into closer proximity, enabling more efficient activation by the altered chain network when subsequently drawn at room temperature. (b) In contrast, shear between two parallel surfaces, separated by a constant height H, due to displacement X, suffers no contraction in the YZ cross-sectional area, as shown in (b'). The lack of condensation of load-bearing strands (solid circles) in YZ plane preserves the areal density of load-bearing strands so that there is no geometric condensation effect in the pre-sheared specimen.

The closer proximity of LBSs due to the geometric condensation has been interpreted to enable more efficient activation of the glassy state when drawn in the same direction as the pre-melt stretching direction:[9] There are more LBSs in displacement during drawing to bring about mobility in the surrounding segments so that the overall molecular mobility can match the imposed drawing rate before breakdown of the chain network. This idea explains why brittle polystyrene (PS) and poly(methyl methacrylate) (PMMA) turns ductile upon adequate pre-melt stretching,[7] an effect known[29-31] since 1960. A similar effect can be brought about by pre-biaxial melt extension. While pre-melt stretched PLA requires geometric condensation to turn ductile, pre-shear can be expected not to result in any improvement of ductility in PLA, highlighting the important difference between various forms of pre-melt-deformation.

# 3. Methods and Materials

## 3.1. Sample Preparation

For squeezing experiments, PLLA square rods were prepared from pellets (NatureWorks, Ingeo 3100HP, MFI = 24 g/10 min at 210 °C, Tg 60 °C) through melt-compression using a Carver Press at 200 °C for 5 minutes at 0.20 MPa and then immediately quenched in ice-water to generate transparent amorphous specimens. The square rods were sanded down with a belt sander until the dimensions were $L_0 \times W_0 \times 2h_0 \sim 27 \times 5 \times 3$ or $55 \times 5 \times 3$ mm$^3$. The resultant rough surface texture brought about by sanding facilitated the marking of the specimens with evenly spaced black marks to quantify the degree of slip and extension along the specimen surface. Amorphous PET (Tg 70 °C) square rods provided by Indorama were likewise sanded down with a belt sander to produce similarly sized specimens. Inspection of the PLLA and PET specimens after sanding by wide-angle x-ray diffraction (WAXD) showed that the prepared PLLA and PET specimens were amorphous.

For uniaxial melt extension experiments, we prepared dogbone-shaped specimens of PLLA and PET through melt compression of PLLA and PET pellets at 200 and 300 °C, respectively, for 5 minutes at 0.20 MPa. Afterwards, specimens were immediately quenched in ice-water to obtain transparent specimens. Subsequent inspection by WAXD showed that the prepared specimens were amorphous. The dogbone specimens have narrow dimensions $L_0 \times W_0 \times D_0$ of $20 \times 10 \times 1.4$ mm$^3$, unless otherwise specified.

## 3.2. Methods

### 3.2.1 Uniaxial Extension

To achieve extensional deformation, dogbone-shaped specimens were drawn above $T_g$ in a pre-heated oven mounted on an Instron tensile tester. The rates and temperatures employed are described in the figure captions, but, in general, deformation temperatures above $T_g$ were selected to avoid quiescent crystallization that could take place during the initial conditioning period and subsequent deformation steps. After extension, specimens were quenched with ice water to prevent additional crystallization and shrinkage upon removal from the oven. After inspection, these melt-stretched specimens were then annealed while constrained along both ends. Specimens prepared through extension have the prefix “ms” (melt-stretched). The prefix “ms-ncc” is used if the specimen developed crystallinity as a result of the melt-stretching or subsequent annealing.

### 3.2.2 Squeezing

Similar principles were applied to achieve shear deformation using the device shown in Fig. 1. In the device, the width dimension was confined by two sidewalls. Pressure was applied topside to force the material out of the trough along the length direction to achieve shear deformation. Prior to sample conditioning, the squeezing device was pre-heated in the oven to the desired temperature for deformation, a process which took 3 hours to achieve from room temperature. The temperature of the squeezing device was determined using a thermocouple that was embedded within one of the side walls. A second thermocouple was used to monitor the air temperature within the oven.

After preheating the device, the specimen was loaded and allowed to condition for 3-8 minutes while in contact with all parts of the device to bring the specimen to the target temperature

and allow for adsorption to the surfaces of the device. After conditioning, a constant squeezing rate $\dot{\imath}$ was applied until a target squeezing ratio $h_0/h$ was met, beyond which the specimen was allowed to anneal while constrained within the device. At the onset of this annealing step, the oven temperature was raised by 20-30 °C in order to accelerate the annealing process. The oven air temperature reached this higher temperature in 15 minutes, whereas the temperature within the device gradually crept to the higher temperature over 30-45 minutes. The target squeezing ratio $h_0/h$ was kept constant during annealing. Specimens prepared using the squeezer have the prefix "msq" (melt-squeezed). The prefix "msq-ncc" refers to pre-melt squeezed specimen that developed NCC after annealing.

### 3.2.3 Atomic force microscopy

After deformation, the specimens from extension and squeezing were inspected by atomic force microscopy (AFM). For AFM measurements, the sample surfaces at the positions marked by the green arrows in Figs. 6-7 were cryo-sectioned by using a Leica UC7/FC7 cryo-ultramicrotome equipped with a Crion anti-static device. For consistency, the processing temperature was set at ~50°C below the nominal glass transition temperature of each material. A Diatome diamond trimming tool (Model: Trim 20) was used to trim the material surface into a pyramid shape with a square block-face of 300µm x 300µm. The top surface was later polished with a fine cryo-diamond knife (Model: Cryo 35°) at 1 mm/sec trimming speed to create a smooth flat surface for the subsequent AFM study. The microtomed specimens were inspected by a Bruker Dimension Icon AFM using the PeakForce QNM (Quantitative Nano-Mechanical characterization) mode, where topography, modulus, adhesion, and dissipation mappings were obtained simultaneously with a single scan. AFM imaging was performed above the $T_g$ of PLA and PET with RTESPA-150 probes (spring constant 5 N/m, resonance frequency 150 kHz, tip radius 8 nm) so that there would be sufficient contrast between the amorphous and crystalline regions.

### 3.2.4 Wide-Angle X-Ray Diffraction (WAXD)

The extent of crystallinity in the specimens before and after extension and squeezing were determined by WAXD at the positions denoted in Figs. 6-8. WAXD patterns were obtained with a rotating anode X-ray generator (RU 300, 12 kW, Rigaku, Woodlands, TX), which produced a beam of monochromatic Cu Kα radiation (λ = 1.54 Å). The X-ray generator operated at 40 kV and 30 mA, and a 0.8 mm diameter collimator was employed. The acquisition time for each specimen was 1 minute and all scans were conducted at room temperature. Two-dimensional (2D) profiles were obtained through transmission mode, with the specimens oriented so that the XY face was normal to the beam direction (i.e., the beam traveled through Z). For clarity, all 2D WAXD images in Section 4 are shown alongside a photograph of the relevant specimen, with the directionality defined for both images by a single set of axes. For example, in Fig. 6(a) the X direction is horizontal for both the specimen image and its accompanying 2D WAXD scan.

From the 2D WAXD images, one-dimensional (1D) profiles of Intensity vs. $2\theta$ were obtained by integrating the intensity over the azimuthal. From these 1D profiles (cf. Fig. 4), the percent crystallinity was obtained by a curve-fitting procedure. For PLA, the peaks between $2\theta$ = 5° to 35° were fitted to Gaussian curves with the peak analysis tool in OriginPro software. The ratio of the area of crystalline peaks seen at $2\theta$ = 16.7°, 18.9°, 24.6°, and 29.0° to the total area under the 1D curve provides the percent crystallinity of PLA.

For PET, peak fitting was accomplished by fitting the shape of the 1D WAXD pattern of an amorphous PET specimen to the corresponding crystalline PET pattern in order to determine the area of the crystalline peaks seen at $2\theta$ = 17.8°, 23.4°, and 25.9°. The ratio of the area of crystalline peaks to the total area under the curve from $2\theta$ = 10° to 35° provides the percent crystallinity of PET.

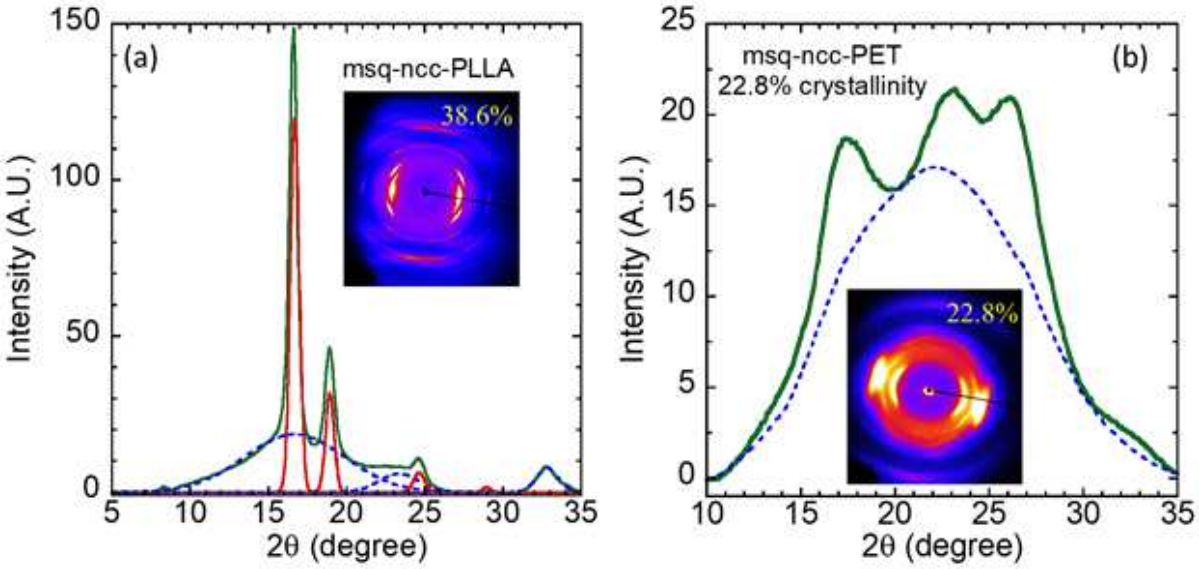


**Figure 4** 2D and 1D WAXD patterns of (a) crystalline PLLA from Fig. 6(b), and (b) PET from Fig. 7(b). The amorphous peaks are denoted by dashed blue lines and the crystalline peaks by solid red lines. (a) For PLLA, the amorphous and crystalline areas were obtained through the Gaussian peak fitting tool of OriginPro software. (b) For PET, the amorphous area was determined by fitting the shape of the 1D WAXD profile of amorphous PET (blue dashed line) to that of the crystalline PET.

### 3.2.5 Small-Angle X-Ray Scattering (SAXS)

After inspection by AFM, specimens were inspected by SAXS. SAXS experiments were performed at room temperature with a Xenocs Xeuss 3.0 instrument using a Cu K$\alpha$ source ($\lambda$ = 1.54 Å) with a beam cross-section of 0.7 mm × 0.7 mm at the specimen position. The X-ray generator operated at 50 kV and 0.6 mA. The sample-to-detector distance was 900 mm for PLA and 370 mm for PET, and the acquisition time for each specimen was 1 hour.

For SAXS measurements, a small layer was sectioned off the specimens that had been previously used for AFM imaging by using a razor blade. The specimen slice was then adhered to a mount with tape. 2D profiles were obtained through transmission mode, with the specimens oriented so that either the XZ or YZ faces were normal to the beam direction (i.e., the beam traveled through Y or X, respectively). The 2D profiles were azimuthally averaged to produce the 1D profiles. The 1D profiles obtained directly from the instrument are presented in Section 4. Comparison to the background 1D profile (i.e., a scan with just the mounting tape) to a typical profile of the PLLA and PET used in this study (cf. Fig. 5) shows a single peak between the regions defined by the direct beam and the signal from the mounting tape.

To determine the long period, the data in Fig. 5 were fit to a Gaussian curve using the peak analysis tool in OriginPro software. The baseline for such peak fitting (shown in the inset of Fig. 5)

was chosen by drawing a line (green dashed line) between the two local minima on either side of the peaks marked with the thick red arrow in Fig. 5. The peak analysis tool provided the position of the peak maximum $q_{max}$, which was used to calculate the long period $L_p = 2\pi/q_{max}$.

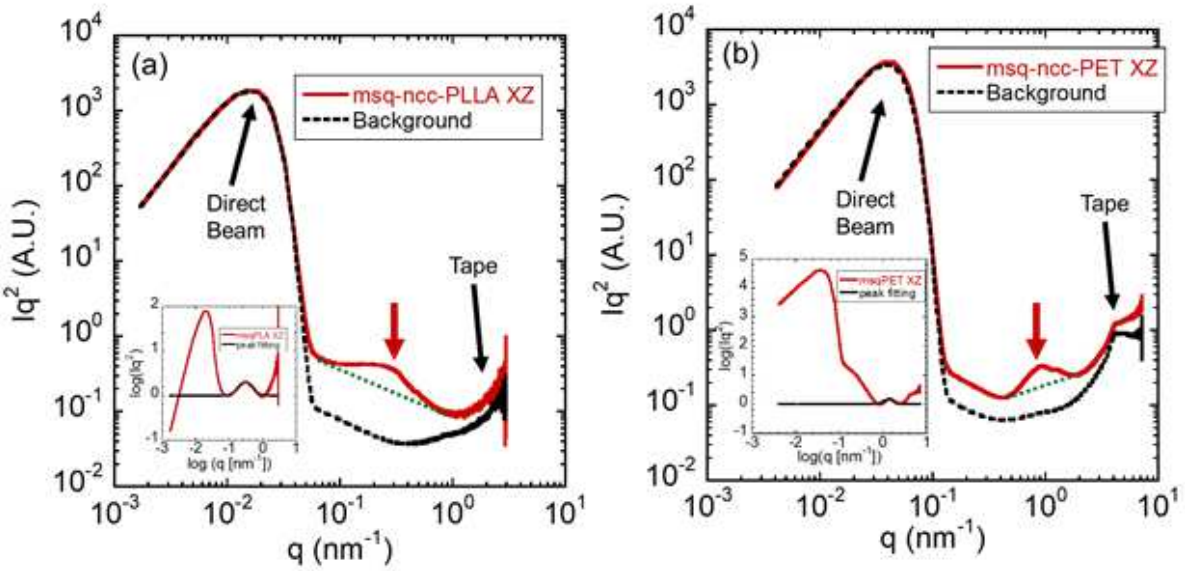


**Figure 5** 1D profiles of PLLA (a) and PET (b). Comparison to the background intensity (black dashed line), which was normalized to match the same maximum intensity as that of the specimen, reveals the presence of a single peak in each specimen, which is marked by the thick red arrow at *ca.* q = 0.3 $nm^{-1}$ for PLLA and *ca.* q = 1 $nm^{-1}$ for PET. The intense signal at the far left is attributed to the direct beam and the noisy, monotonically increasing signal along the far right is attributed to the mounting tape. The green dashed line shows the baseline that was used for the subsequent $q_{max}$ determination in the insets. The insets of (a) and (b) show the specimen signal (red line) after baseline correction and the Gaussian peak fit (dashed black line) that was used to determine $q_{max}$.

## 4. Experimental results

Large pre-melt deformation in the elastic (i.e., affine) limit, i.e., for Weissenberg number much greater than unity, has been predicted[10] to induce nano-confined (cold) crystallization (NCC) in class B semicrystalline polymers (i.e., crystallizable polymers with $T_g$ above room temperature). Large pre-melt deformation in the elastic (i.e., affine) limit, i.e., for Weissenberg number much greater than unity, has been predicted[10] to induce nano-confined (cold) crystallization (NCC) in class B semicrystalline polymers (i.e., crystallizable polymers with $T_g$ above room temperature). As reference, we show in Fig. 6(a) AFM evidence of NCC in PLLA along with the stress vs. strain curve associated with the pre-melt stretching done at 10 degrees above $T_g$, i.e., at ca. 70 $^{o}$C. Specifically, the AFM images in two planes reveal the isotropic (YZ plane) and anisotropic (XZ) morphologies, respectively. The white strings in XZ plane represent NCC because NCC can be expected to be stiffer than the amorphous rubbery phase (darker regions), as the AFM measurements were carried out above $T_g$. These NC crystals appear to form a percolative network with preferential orientation. Moreover, these crystals align perpendicular to the pre-melt-stretching direction (X axis), to suggest kebab-like crystalline morphology induced by the chain orientation along X axis. The "kebabs" are

separated by an average distance which is the long period, $L_P$ = *ca.* 20 nm, where an average width of the strings shows a kebab "thickness" $L_K$ = *ca.* 4 nm. The YZ-plane AFM image confirms the cylindrical symmetry expected from the cross-section of uniaxial extension. Finally, WAXD 2D scan in Fig. 6(a) shows the expected alignment of crystalline morphology.

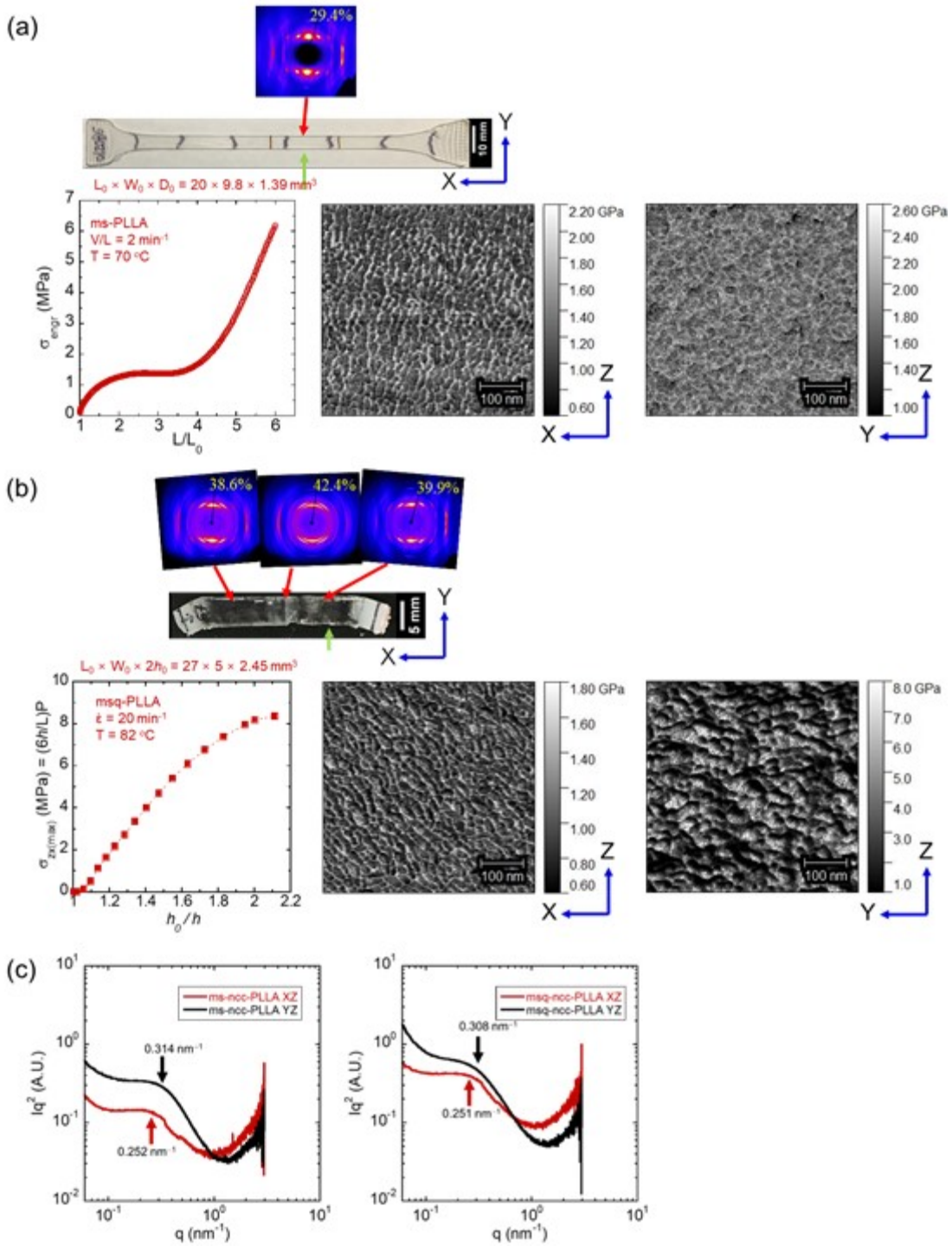


**Figure 6** (a) Stress vs. strain curve from uniaxial melt-stretching at V/L = 2 min$^{-1}$ at 70 °C to λ = 6 of amorphous PLLA (aPLLA), followed by ice water spray and subsequent annealing at 61-63 °C for 1000 s with both ends constrained. AFM scans of the resulting ms-ncc-PLLA, taken at 80 °C, in both XZ and YZ planes, reveal morphological features on nanoscopic scales. (b)

Stress vs. strain curve from melt squeezing at $\dot{\varepsilon}$ = 20 min$^{-1}$ to $h_0/h$ = 2.0 of aPLLA specimen, after thermal equilibration in the squeezing device at 82 °C for 6 minutes. Photo taken against a dark background shows opaqueness in the middle and two ends of the specimen that had been squeezed out of the trench, and transparency away from the middle. The WAXD scans in (a) and (b), taken with the x-ray beam traveling along Z in the middle of the specimen at the positions marked by the red arrows, reveal both types of crystallization. The degree of crystallization is indicated in the 2D scans. AFM scans taken at 80 $^{o}$C along the XZ and YZ planes (at the positions marked by the green arrows) show nanoscopic morphology similar to those in (a). (c) SAXS plot of the same samples examined in (a) and (b), obtained in the manner described in Section 3.2.5. The low q region containing the x-ray beam (q < 0.06 nm$^{-1}$) is not shown to emphasize the signals that come from the specimens. The peak maximum $q_{max}$ is shown for each peak along with the q value. The signals reveal a structure *ca.* 0.25-0.31 nm$^{-1}$, which corresponds to a long period spacing of 20-25 nm, consistent with the AFM scans.

According to our theoretical analysis of Section 2, melt squeezing in the trough depicted in Fig. 1 should produce significant shear deformation near the two exits and little shear deformation in the middle. After melt squeezing as described in the caption of Fig. 6(b), without unloading the squeezed PLLA was annealed for 40 minutes to induce NCC by setting the oven to 100 °C at the start of the annealing. Both NCC and conventional crystallization occurred in different sections (transparent – NCC and opaque – conventional crystallization) along the specimen. Also opaque are the two portions outside of the trough that also underwent conventional spherulitic crystallization. The corresponding shear stress can be evaluated according to Eq. (8) from the pressure P measured by the load cell of the Instron tensile tester, as shown in Fig. 6(b). According to our analysis in Section 2 there is only weak melt extension, and the degree of shear deformation grows from the middle toward the edges. WAXD 2D scans in Fig. 6(b) confirm this trend: lower degree of orientation in the middle of the specimen based on the appearance of more observable rings. More importantly, AFM imaging reveals NCC in both XZ and YZ planes. The AFM image in XZ plane is particularly noteworthy: The shear deformation induces formation of NCC that orients at a large angle with respect the shearing direction of the X axis. In other words, the NC crystals are no longer vertical, as seen in Fig. 6(b), but at an angle to the X axis.

SAXS measurements were carried out to verify the emergence of NCC in the pre-melt deformed PLLA that had subsequently undergone annealing to induce NCC. Fig. 6(c) indeed suggests that there is a crystalline structure on the length scale of 20-25 nm, in agreement with what is observed from the AFM scans.

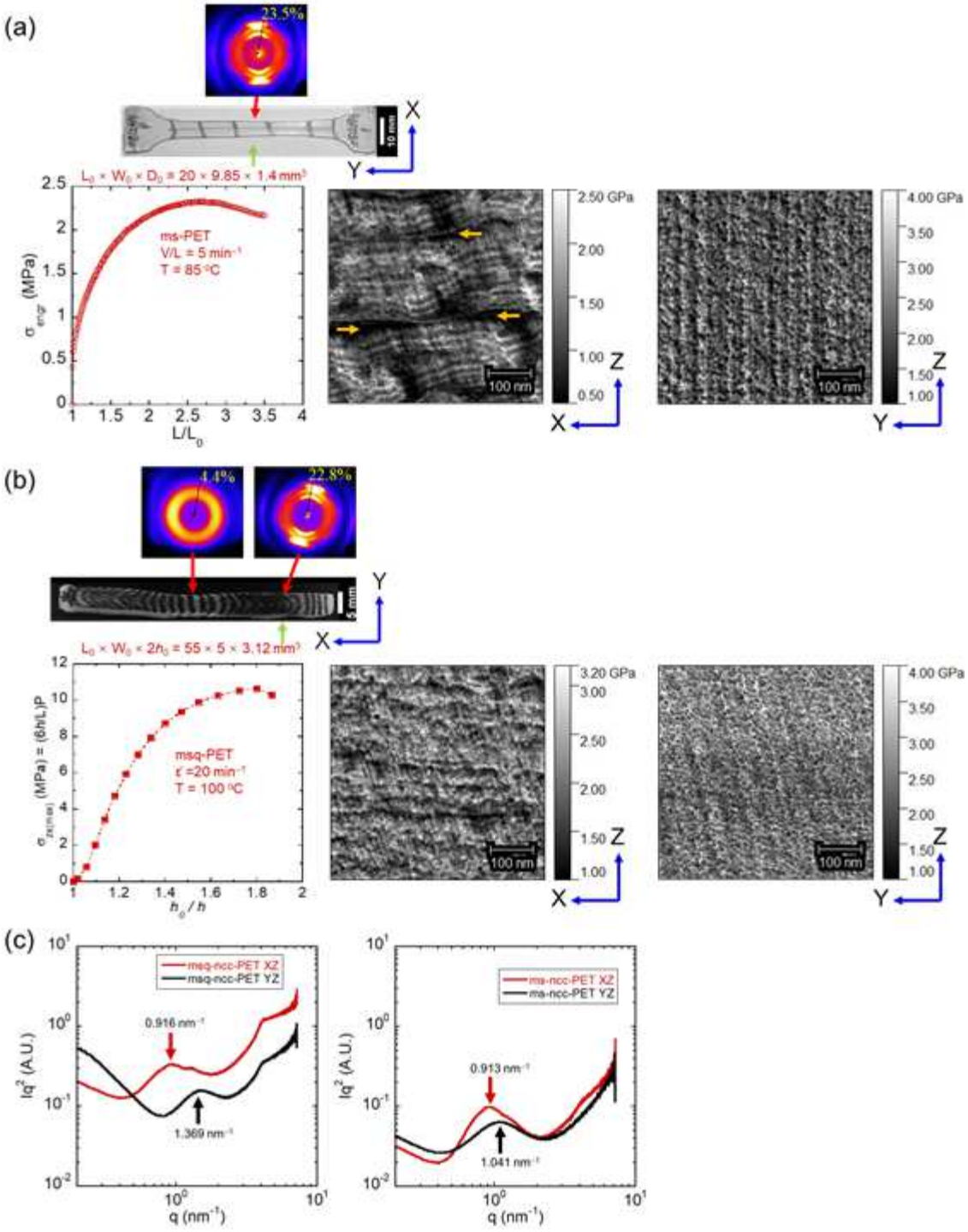


**Figure 7** (a) Stress vs. strain curve from uniaxial melt-stretching at 85 °C with V/L = 5 $min^{-1}$ to $L/L_0$ = 3.5 of aPET specimen, followed by ice water spray and subsequent annealing for 45 minutes, during which the temperature slowly rose from an initial 85 °C to 115 °C at the end of annealing. (b) Stress vs. strain curve from melt squeezing at 100 °C at $\dot{\varepsilon}$ = 20 $min^{-1}$ to $h_0/h$ = 1.8 of aPET specimen. After squeezing, the specimen was annealed under constraint for 35 minutes at 100 °C to allow the specimen to crystallize. Photo taken against a dark background shows opaqueness in the middle and two ends of the specimen that had been squeezed out of the trench, and transparency away from the middle. In both (a) and (b),

AFM scans, taken at 80 °C in both XZ and YZ planes (at the positions marked by the green arrows), and WAXD scans, taken with the x-ray beam traveling along Z in the middle of the specimen at the positions marked by the red arrows, show morphologies similar to those of PLLA in Fig. 6(a)-(b). In (a), the specimen is very weak along the transverse direction, as evidenced by the spontaneous formation of cracks during cutting of the specimen with scissors. As such, the low modulus regions (dark regions indicated by orange arrows) in the XZ scan are believed to originate from microcracks, though when exactly they appeared during specimen preparation is presently unknown. (c) SAXS plot of the same samples examined in (a) and (b), obtained in the manner described in Section 3.2.5. The low q region containing the x-ray beam ($q < 0.2$ nm$^{-1}$) is not shown to emphasize the signals that come from the specimens. The peak maximum $q_{max}$ is shown for each peak along with the q value. The signals reveal a structure *ca.* 0.9-1.4 nm$^{-1}$, which corresponds to a long period spacing of 4.6-6.9 nm, which is slightly shorter than the 7-13 nm observed with the AFM scans.

To demonstrate the universality of our understanding regarding pre-melt-deformation induced NCC in class B semicrystalline polymers, we have carried out a parallel study based on PET. First, we confirm that pre-melt stretching can induce NCC during annealing as shown in Fig. 7(a) by the AFM images, along with the stress vs. strain curve from pre-melt-stretching test. Second, PET is subjected to melt squeezing as shown in Fig. 7(b) to a ratio of $h_0/h = 1.8$. The photo in Fig. 7(b) shows once again that the middle appears opaque, as are the two ends that had been squeezed out of the trough. WAXD scans indicate the relative isotropic crystallization at the middle and oriented NCC near the two ends of the specimen. AFM confirms nanoscopic morphology to suggest formation of NCC. As in the case of PLLA, the SAXS measurements in general agree with the AFM measurement.

Finally, width of WAXD peaks can be analyzed based on Scherrer equation of both NCC-containing and conventional cold crystallized PLA and PET. The analysis shows NCC state has broader width, corresponding to smaller grain sizes, i.e., lower dimensions along the respective crystallographic phanes, at most by a factor of two, relative to the cold crystallized samples.

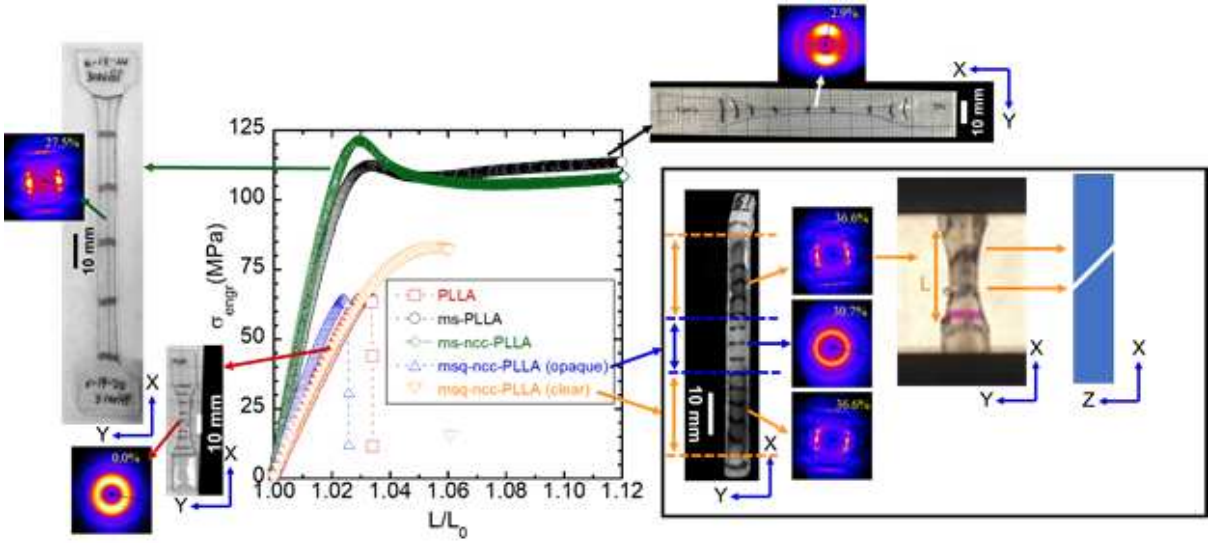

**Figure 8** Stress-strain curves for room-temperature extension of PLLA and ncc-PLLA prepared through melt-extension (ms-ncc) and melt-squeezing (msq-ncc). Specimens were drawn at $V_0$ = 5 mm min$^{-1}$ to failure. PLLA (□) dogbone showed brittle failure. Ms-PLLA (■) was prepared by melt-stretching a dogbone of $L_0 \times W_0 \times D_0$ = 14 × 4.5 × 2.9 mm$^3$ at V/L = 2 min$^{-1}$ to $L/L_0$ = 2.9 at 69 °C, spraying with ice water to prevent further crystallization, cut into a stripe with gage dimensions of $L_0 \times W_0 \times D_0$ = 47 × 2.2 × 1.4 mm$^3$, then drawn to failure to $L/L_0$ = 1.26. Experimental details for the other specimens are discussed in the main text. The ms-PLLA and ms-ncc-PLLA specimens did not show necking during drawing. The msq-ncc-PLLA photo taken against a dark background shows opaqueness in the middle (between blue dashed lines) and two ends of the specimen that had been squeezed out of the trench (above and below orange dashed lines), and transparency away from the middle (between blue and orange dashed lines). WAXD scans, taken with the beam traveling along Z in the middle of the specimens, were taken at the positions marked by the arrows on the respective specimens.

Beyond demonstrating the formation of NCC through shear-induced melt-deformation, it is instructive to find out whether the msq-ncc-PLLA remains brittle despite pre-deformation. PLA in its isotropic amorphous form is brittle at room temperature. In its glassy state the polymer is presumably deeply trapped in its energy minimum. In other words, at room temperature the chain network is inadequate[9] to bring about activation and cause yielding during uniaxial drawing. Conventionally, crystallized PLLA is just as brittle as amorphous PLA, showing weak mechanical strength because isothermal crystallization supposedly only further weakens the chain network by depleting chain uncrossability that is essential for chain networking. Robust networking is necessary for yielding to prevail so that brittle fracture can be avoided according to the recent picture.[9] Specifically, Ref. [9] explained how geometric condensation (cf. Fig. 3) achieved through pre-melt stretching can enhance the chain network and turn an otherwise brittle glassy polymer ductile.[7]

It is instructive to compare mechanical characteristics of NCC-containing PLA where NCC formation involves different types of pre-melt deformation. First, melt-stretching induced NCC (◇) is prepared by drawing a dogbone involving a rectangle shaped narrow section with $L_0 \times W_0 \times D_0$ = 20 × 9.9 × 1.5 mm$^3$ at V/L = 1.62 min$^{-1}$ to $L/L_0$ = 4 at 72 °C and then immediately annealing without unloading for 15 minutes to induce NCC. The specimen (ms-ncc-PLLA) was then cut into a stripe of $L_0 \times W_0 \times D_0$ = 36.6 × 5.1 × 0.69 mm$^3$ and drawn at $V_0$ = 29.3 mm min$^{-1}$ to failure at $L/L_0$ = 1.49 (Video 1). For reference, the same pre-melt-stretched amorphous PLLA, without annealing to induce NCC, was also drawn. The stress vs. strain curves in Fig. 8 indicate that ms-PLLA (amorphous) as well as ms-ncc-PLLA are strong and ductile, unlike the untreated PLLA in squares, which is weak and brittle. The comparable mechanical response of ms-PLLA and ms-ncc-PLLA confirms that NCC has preserved the effect of geometric condensation: a "geometrically condensed" chain network can turn PLA from brittle to ductile,[3] similar to the case of PS.[7, 9]

Second, shear-induced NCC in PLLA is achieved using melt squeezing in the setup depicted in Fig. 1 after thermal equilibration for 3 minutes at 72 °C. The specimen fit into the trough had initial dimensions of $L_0 \times W_0 \times 2h_0$ = 55 × 5 × 2.75 mm$^3$. The melt squeezing was carried out at $\dot{h}$ = 2 min$^{-1}$ to $h_0/h$ = 2.0, followed by annealing for 80 minutes. At the onset of annealing, the oven temperature was increased to 80 °C, then changed again to 110 °C after 40 minutes. The resulting

specimen is shown by the photo in Fig. 8. The specimen is optically transparent except for the middle section, indicating that the middle section underwent conventional cold crystallization during annealing. This appearance thus confirms the theoretical analysis in Section 2 that there is little shear deformation in the middle during the squeezing. Specifically, Eq. (6) shows that the shear strain linearly increases from zero in the middle toward the two exits. With sufficient shear deformation away from the middle, NCC occurs so that the specimen shows the expected transparent appearance. While pre-melt shear deformation can induce NCC in PLA, such a heat-resistant PLA should be brittle at room temperature because of lack of geometric condensation. The middle section of the specimen shown in Fig. 8 should be weakest, as it suffered little geometric condensation and experienced conventional crystallization that can weaken the chain network.

The specimen was first drawn at $V_0$ = 5 mm min$^{-1}$ until fracture at the middle into two pieces (Video 2). The corresponding stress vs. strain curve is presented in up-pointing triangles △. Subsequently, we subject one of the two pieces to drawing in order to determine the mechanical response of this piece that had significant shear-induced NCC. To do so, the piece is cut into a dogbone-shaped specimen using a sanding belt to new dimensions $L_0 \times W_0 \times D_0$ of 4.4 × 3.4 × 1.8 mm$^3$ (cf. Fig 8) and then drawn at $V_0$ = 5 mm min$^{-1}$ (Video 3). As shown by down-pointing triangles ▽, the msq-ncc-PLLA is brittle and fails at an angle through the thickness, as depicted in Fig. 8, in sharp contrast with ms-ncc-PLLA. Our explanation is as follows. Since pre-shear-melt deformation does not produce geometric condensation, it cannot improve the ability of the pre-sheared PLLA to undergo yielding at room temperature. Thus, this comparison between ms-ncc-PLLA and msq-ncc-PLLA underscores the importance and necessity to alter chain network structure by geometric condensation for a brittle glassy polymer (e.g., the present PLLA), either amorphous or NCC-containing, to turn ductile.

## 5. Summary

The present study differs from such large topics as (1) flow-induced crystallization, which concerns itself with the processing-structure relation, and (2) deformation mechanism and structural changes associated with large extension of semicrystalline polymers, which probe the structure-property relationship. Our aim is to show how the processing-structure-property relationship can be explored all together. Specifically, we show that nano-confined crystallization (NCC) in PLA and PET, evidenced by AFM imaging and SAXS data, can be induced by various forms (shear and uniaxial and biaxial stretching) of pre-melt deformation, confirming the theoretical prediction that chain orientation in an elastically deformed chain network may induce crystallization to take place at the network mesh size scale. The resulting NCC-containing PLA and PET show different mechanical characteristics at room temperature, i.e., their glassy state. Specifically, the introduction of pre-shear in PLA allows us to establish the unique importance of melt extension: In absence of geometric condensation that can only be introduced through uniaxial and biaxial extensions, the ductility of a glassy polymer cannot improve. In other words, since shear does not alter the chain network in such a way as to bring the network strands physically closer to enhance molecular activation, pre-shear PLA remains brittle. This finding emphasizes the important insight from a recent molecular picture that[9] the geometric condensation is necessary to alter the mechanical response of brittle glassy polymers such as PS, PMMA and PLA. In other words, our experiments has

for the first time explicitly identified what type of pre-melt deformation is required to change the chain network structure so as to affect the mechanical response of the processed (otherwise brittle) polymers. While NCC is an attractive feature allowing heat distortion temperature to be significantly elevated and sample to retain optical clarity, it does not improve ductility. Only a certain type of processing, e.g., uniaxial or biaxial melt stretching, can produce favorable structural changes to ensure that the mechanical properties can be greatly improved. Pre-melt-stretched PLA shows a successful example of improved processing-structure-property relationship for semicrystalline polymers.

## Acknowledgements

This work is supported, in part, by a grant from the Polymers program of the National Science Foundation (DMR-1905870) as well as ACS-PRF (60897-ND7). Microtome work was conducted at the Advanced Materials and Liquid Crystal Institute in Kent State University. Atomic force microscopy scans and analysis was performed at the School of Polymer Science and Polymer Engineering at the University of Akron. SAXS results were obtained in the X-ray scattering facility at the Advanced Materials and Liquid Crystal Institute (AMLCI) at Kent State University, which was financially supported by the National Science Foundation (DMR-2017845), the State of Ohio (The Ohio Department of Higher Education Action Fund), and Kent State University.

## References


[1] L. Mandelkern, F. L. Smith, M. Failla, M. A. Kennedy, A. J. Peacock, *Journal of Polymer Science Part B: Polymer Physics* **1993**, *31*, 491.
[2] G. W. T. Ehrenstein, R. P., "*Polymeric Materials: Structure, Properties, Applications*", Hanser Gardner Publications, Munich : Hanser; Cincinnati, OH, 2001.
[3] M. Razavi, S.-Q. Wang, *Macromolecules* **2019**, *52*, 5429.
[4] A. van der Wal, J. J. Mulder, H. A. Thijs, R. J. Gaymans, *Polymer* **1998**, *39*, 5467.
[5] P. I. Vincent, *Polymer* **1972**, *13*, 558.
[6] H. Chen, M. Pyda, P. Cebe, *Thermochimica Acta* **2009**, *492*, 61.
[7] G. D. Zartman, S. Cheng, X. Li, F. Lin, M. L. Becker, S.-Q. Wang, *Macromolecules* **2012**, *45*, 6719.
[8] S.-Q. Wang, "*Nonlinear Polymer Rheology: Macroscopic phenomenology and Molecular foundation*", Wiley, Hoboken, NJ, 2018.
[9] S.-Q. Wang, S. Cheng, P. Lin, X. Li, *The Journal of chemical physics* **2014**, *141*, 094905.
[10] M. Razavi, W. Zhang, H. A. Khonakdar, A. Janke, L. Li, S. Q. Wang, *Soft Matter* **2021**, *17*, 1457.
[11] K. N. Okada, J. Washiyama, K. Watanabe, S. Sasaki, H. Masunaga, M. Hikosaka, *Polymer Journal* **2010**, *42*, 464.
[12] K. Okada, Y. Tanaka, H. Masunaga, M. Hikosaka, *Polym. J.* **2018**, *50*, 167.
[13] R. H. Somani, B. S. Hsiao, A. Nogales, S. Srinivas, A. H. Tsou, I. Sics, F. J. Balta-Calleja, T. A. Ezquerra, *Macromolecules* **2000**, *33*, 9385.
[14] R. H. Somani, B. S. Hsiao, A. Nogales, H. Fruitwala, S. Srinivas, A. H. Tsou, *Macromolecules* **2001**, *34*, 5902.
[15] R. H. Somani, L. Yang, L. Zhu, B. S. Hsiao, *Polymer* **2005**, *46*, 8587.
[16] S. Kimata, T. Sakurai, Y. Nozue, T. Kasahara, N. Yamaguchi, T. Karino, M. Shibayama, J. A. Kornfield, *Science* **2007**, *316*, 1014.
[17] A. Pawlak, A. Galeski, A. Rozanski, *Progress in Polymer Science* **2014**, *39*, 921.
[18] Y. Lu, Y. Men, *Macromolecular Materials and Engineering* **2018**, *303*, 1800203.
[19] A. Peterlin, *J Mater Sci* **1971**, *6*, 490.
[20] A. Galeski, *Progress in Polymer Science* **2003**, *28*, 1643.
[21] D. Y. Yoon, P. J. Flory, *Faraday Discussions of the Chemical Society* **1979**, *68*.
[22] M. A. Kennedy, A. J. Peacock, L. Mandelkern, *Macromolecules* **1994**, *27*, 5297.
[23] F. Zuo, J. K. Keum, X. Chen, B. S. Hsiao, H. Chen, S.-Y. Lai, R. Wevers, J. Li, *Polymer* **2007**, *48*, 6867.
[24] R. J. Young, P. B. Bowden, *J Mater Sci* **1973**, *8*, 1177.
[25] R. J. Young, P. B. Bowden, J. M. Ritchie, J. G. Rider, *J Mater Sci* **1973**, *8*, 23.
[26] X. Li, S.-Q. Wang, *J Rheol* **2018**, *62*, 491.
[27] R. Yuan, S.-Q. Wang, *J Rheol* **2020**, *64*, 1251.
[28] R. S. Tsai, D. K. Lee, H. Y. Fang, H. B. Tsai, *Asia - Pacific Journal of Chemical Engineering* **2009**, *4*, 140.
[29] G. Gruenwald, *Modern Plastics* **1960**, *38*, 137.
[30] D. H. Ender, R. D. Andrews, *Journal of Applied Physics* **1965**, *36*, 3057.
[31] C. B. Bucknall, "*Toughened plastics*", Springer, 1977.

Both pre-extension and pre-shear of amorphous PLA and PET above their $T_g$ in the affine deformation limit can induce nano-confined crystallization (NCC), with crystal sizes limited to nanoscopic scale so as to render the processed PLA and PET optically transparent. It is shown that a certain type of deformation (pre-extension) is required to turn brittle PLA ductile.